Adsorption Heterogeneity of Lysozyme Over Functionalized Mesoporous Silica: Effect of Interfacial Noncovalent Interactions

Jing He, Zhijun Liu, and Chunxi Hai
State Key Laboratory of Chemical Resource Engineering, Beijing University of Chemical Technology, Beijing 100029, P.R. China

DOI 10.1002/aic.11561
Published online July 11, 2008 in Wiley InterScience (www.interscience.wiley.com).

In this work, the surface–protein interfacial noncovalent interactions are generated and tuned as hydrogen bonding, hydrophobic affinity, electrostatic interaction, and additional π-π overlapping through designing suitable surface property with different chemical moieties and varying the pH of adsorption medium. The heterogeneity of lysozyme (Lz) adsorption is investigated. It has been found that the interfacial interactions of support surfaces and the protein play a key role in the adsorption kinetics, adsorption capacity, distribution states, and adsorption reversibility of Lz, while the protein–protein repulsion makes impact dependently on the nature of surface–protein interactions. The π-π overlapping is another significantly crucial driving force in addition to the electrostatic force, hydrophobic interaction, and hydrogen bonding that commonly drive protein adsorption. But the hydrogen bonding between surface NH_2 and Lz is exceptionally not sufficient to drive Lz adsorption. The adsorption of Lz on functionalized mesoporous silica is partial reversible and makes no damage on the protein secondary structure. © 2008 American Institute of Chemical Engineers *AIChE J,* 54: 2495–2506, 2008

Keywords: interfacial interaction, noncovalent, protein adsorption, surface functionalization, mesoporous materials

Introduction

The uniform pore diameters larger than zeolites, huge surface areas, high pore volumes, and good chemical and mechanical stabilities of mesoporous silica materials[1–8] open up their attractive application as hosts for immobilization and separation of large guests, especially bioactive molecules. In the decade since the first report of adsorption of globular protein[9] on mesoporous material, different kinds of proteins on various mesoporous materials have been reported, as reviewed recently by Hartmann.[10] Considering different applications such as separation, biocatalysis, biosensors, and controlled release and delivery, the adsorption heterogeneities of proteins including adsorption capacity, permanent or reversible features, and protein distribution are needed. For instance, rapid permanent monolayer adsorption is preferred for a biocatalyst, while as little as possible irreversible adsorption on chromatographic supports is required for bioseparation. Thus, understanding the adsorption heterogeneity of proteins on mesoporous hosts, as well as its depending factors and tunable extension, is of great importance.

The major factors that might influence the adsorption heterogeneities of proteins in mesoporous hosts involve spatial

Correspondence concerning this article should be addressed to J. He at jinghe@263.net.cn.

factors and interfacial interactions. Size selectivity of mesoporous hosts has been extensively discussed by several groups.[9,11–17] Additionally, by carefully controlling the morphology of hexagonal mesoporous silica, Fan et al.[18] found that SBA-15 with smaller particle size possessed more entrances to entrap lysozyme (Lz) than conventional SBA-15 with larger particle size, leading to much improved bioimmobilization ability and adsorption rate. Very recently, Liu et al.[19] found that the mesoporous nanorods with channels running parallel to the short axis could greatly accelerate the enzyme adsorption. The interfacial interactions between proteins and support surfaces are more complex than spatial factors. Interfacial interactions between proteins and mesoporous hosts mainly contain covalent and noncovalent forces. Usually, the host–guest covalent interactions that result from fiercely interfacial chemical reactions and format a new molecule lead to irreversible protein adsorption.[14] This strong interaction could easily provide a stable immobilized enzyme system.[20] The noncovalent interactions[21] extensively existing in the biomacromolecules such as DNA and proteins, which lead to the formation of the host–guest or guest–guest clusters, are supposed to play an important role in adsorption heterogeneities of proteins. Even though not well-defined, the typical noncovalent interactions[21] include hydrogen bonding, electrostatic, hydrophobic, and some specific noncovalent forces. So charge features and hydrophobicity of solid surfaces, isoelectric points of proteins, as well as pH and ion strength of adsorption medium might dependently influence the interfacial noncovalent interactions.[22] Several researchers reported the effects of electrostatic interactions on protein adsorption heterogeneity.[16,17,23–27] Hudson et al.[26] found that there was practically no adsorption for cyt c and xylanase onto SBA-15 when the ionic strength was increased to higher than 0.5 M, implying the dominant electrostatic interactions. By incorporating aluminum into pure silica materials, the adsorption amounts of cyt c[17] and Lz[27] increased, and this observed increase was most likely a consequence of strong electrostatic interaction between the negative charges on the aluminum sites and the positively charged amino acid residues of the proteins. Through careful tuning of the solution pH, Vinu et al. found that the maximum loadings of cyt c[17] and Lz[24,27] on siliceous, Al-containing, and carbon nanoporous materials were all achieved near the protein isoelectric points. This might result from the zero net charge of proteins, and thus there was no electrostatic repulsion or attraction between amino acid residues, resulting in size reduction of the protein molecules. As for the distribution states of adsorbed proteins, most adsorption isotherms were found to be pseudo-Langmuir type demonstrating a monolayer adsorption.[17,24,27] When the repulsive electrostatic interaction of protein–protein is weaker than that of surface–protein however, Brunauer–Emmett–Teller (BET) type indicative of a multilayer adsorption was observed.[27] Few publications involved the influences of hydrophobicity and hydrogen bonding on protein adsorption heterogeneities.[28–30] But no comprehensive understanding has been reported so far.

In this paper, the surface–protein interfacial noncovalent interactions are generated and tuned through tailoring the surface of mesoporous material (SBA-15 herein) with functional groups (—OH, —CH_6H, —$C_3H_6NH_2$, —$C_3H_6NHCONH_2$, and —C_3H_6COOH) and varying the pH of adsorption medium. The adsorption heterogeneities of Lz over the modified supports, including adsorption capacity, adsorption rate, protein distribution, and adsorption reversibility associated with the surface–protein or protein–protein noncovalent interactions, are especially concerned. The incorporation of organic components into mesoporous silicas permits tuning of the surface properties (hydrophilicity, hydrophobicity, functionality, binding to guest molecules)[31–35] and has been used in the immobilization of bioactive molecules.[30,36,37] There are three approaches to achieve the surface functionalization: postsynthesis grafting of organic components onto a pure silica matrix, simultaneous reaction of condensable inorganic silica species and organic silanes (co-condensation, one-pot synthesis), and usage of bissilylated organic precursors that lead to periodic mesoporous organosilicas.[32–34] Employed in this work is the postsynthesis grafting method, to assure that all the functional groups incorporated are located on the surface.

Depending on the surface groups and operating pH, the potential noncovalent interactions between support surfaces and proteins involved in this work contain hydrogen bonding derived from terminal —Si—OH, —COOH, —NH_2, and —$NHCONH_2$ on support surfaces and —NH_2 or —COOH in proteins, hydrophobic interactions from terminal alkyls on support surfaces, and side chains of amino acid residues in proteins, electrostatic interactions from unprotonated terminal —Si—OH and —COOH, protonated terminal —NH_2 or —$NHCONH_2$ on solid surfaces with charged protein surfaces, as well as π-π overlapping between surface —$NHCONH_2$ and the peptide bonds in proteins. Some specific noncovalent interactions such as alkyl-aromatic ring,[38] C—H···Y (Y = electronegative atom), and C—H···π types[21] are out of discussion in this paper.

Experimental

Materials

Pluronic P123 (M_{av} = 5800, Aldrich), *n*-propyltriethoxysilane (98%, Lot No. P060327012, Jingzhou Jianghan Fine Chemical Co., Ltd.), 3-aminopropyltriethoxysilane (98.5%, Lot No. P060327011, Jingzhou Jianghan Fine Chemical Co., Ltd.), 3-ureidopropyltriethoxysilane (50% in methanol, Lot No. P060327014, Jingzhou Jianghan Fine Chemical Co., Ltd.), 4-(triethoxysilyl)butyronitrile (98%, Aldrich), tetraethoxy-silane (Beijing Chemical Factory), toluene (Beijing Chemical Factory), and benzophenone (Beijing Chemical Factory) are all of analytical purity and used as received (if no further statement). Hen egg white Lz (2× crystallized, lyophilized, 20,000 U/mg of protein) from Sinopharm Chemical Reagent Co., Ltd (Lot No. F20060410) was stored in a 273–277 K refrigerator.

Preparation and modification of SBA-15

SBA-15 was synthesized as reported.[7] The template was removed by calcination at 823 K for 6 h. The calcined SBA-15 was activated using the following procedure[39]: (1) Immerse the mesoporous silica (3.0 g) into a mixture of HCl:MeOH (1:1, v/v) (40 mL) at room temperature for 30 min. Rinse the silica three times with deionized water. (2)

Immerse the silica into 25 mL of concentrated H_2SO_4 (98%) at room temperature for 30 min. Rinse the silica well with deionized water. It is important to remove all H_2SO_4 residues from the solid in order to make a uniform silane monolayer. (3) Boil the silica for 30 min in 150 mL of deionized water. The resulting solid was filtered, dried at room temperature for 12 h, and then at 373 K for 2 h to give activated SBA-15, denoted SBA-OH. Triethoxysilanes $(EtO)_3Si—X$ (X = C_3H_6H, $C_3H_6NH_2$, C_3H_6CN and $C_3H_6NHCONH_2$) were used to generate different properties of silica surfaces. Typically, 1.0 g of SBA-OH, which was pretreated in 423 K oven for 2 h before its usage, was suspended in 40 mL of toluene (99.7%, further distillation by refluxing the mixture of 500 mL toluene, 1 g Na, and 5 mg benzophenone as visual indicator for ~5 h). Then 5 mmol of triethoxysilane (calculated from the maximum grafting amount based on assumption of 5×10^{18} molecules per square meter in a fully dense monolayer coverage)[31] was added. The mixture was refluxed for 24 h. The white solid was filtered, washed with diethyl ether, and dried in air. The samples were denoted SBA-X, where X is the functional group on the surface. SBA-C_3H_6COOH was produced by refluxing SBA-C_3H_6CN in 35.5% (w/w) HCl solution for 24 h.

Characterization

Powder XRD patterns were obtained using a Rigaku D/MAX-2500 X-ray diffractometer (Cu Kα radiation) with a scan rate of 1°/min. The low-temperature (77 K) nitrogen sorption isotherms were measured using a Quantachrome Autosorb-1 system. The pore size distribution was calculated using the BJH (Barrett-Joyner-Halenda) method. The specific surface area was calculated using the BET method. FTIR spectra were recorded on a Bruker Vector 22 spectrometer at 1 cm^{-1} resolution, the samples being pressed into disks with KBr. Scanning electron micrographs (SEM) were taken on a Cambridge S-250MK3 microscope. Transmission electron micrographs (TEM) were taken on a FEI Tecnai 20 electron microscope operating at 200 kV. CHN element analysis was performed on Elementar Vario EL III elemental analyzer. The UV absorption data were collected on a Shimadzu UV-2501 spectrometer. The solid state ^{29}Si MAS NMR spectra were taken at a resonance frequency of 59.6 MHz on a Bruker Avance 300 M solid-state spectrometer equipped with a commercial 5-mm MAS NMR probe. The magic angle spinning frequency was set at 5 kHz. The chemical shift was determined relative to TMS.

Lz adsorption and desorption

Twenty-five millimolar buffer solutions with different pH were first prepared, citric acid–dibasic sodium phosphate buffer for pH = 4.8, potassium dihydrogen phosphate–dibasic sodium phosphate buffer for pH = 6.8, and sodium carbonate–sodium bicarbonate buffer for pH = 10.0 and 12.0. A series of standard Lz solutions with the concentration ranging from 0.2 to 6.0 mg/mL were prepared by dissolving different amounts of Lz in the aforementioned buffers. In the adsorption experiments dealing with adsorption capacity and kinetics, 15 mg of the SBA-X (X = OH, C_3H_6H, $C_3H_6NH_2$, $C_3H_6NHCONH_2$, or C_3H_6COOH) adsorbent was immerged in 10 mL of 1 mg/mL Lz solution and was continuously shaken at 298 K in an oscillator with a speed of 130 shakes/min for 120 h. The mixture was sampled at intervals and centrifuged at 5000 rpm for 10 min to monitor the Lz concentrations in supernatants. Then the supernatant liquids were remixed with the adsorbents by vortex. The adsorbed amount of Lz on mesoporous silica was calculated by subtracting the Lz in supernatant from the total Lz content. The Lz content was determined by UV absorption at 280 nm. In the adsorption pseudo-isotherm experiments for dealing with protein distribution state, 15 mg of the SBA-X adsorbent was immerged in 5 mL of 0.2–6.0 mg/mL Lz solution and was continuously oscillated at a certain temperature for 24 h. In the desoportion experiments, 15 mg of the SBA-X adsorbent was first immerged at 298 K in 5 mL of 0.6 mg/mL Lz solution at pH = 6.8 and 10 for 24 h, respectively. After measurement of the adsorption amount, the washed adsorbent was immerged at 298 K for 24 h in a blank buffer with the same pH as that for adsorption to measure the percentage leaching of Lz.

Results and Discussion

Adsorbent characterization

Considering the comparability and general applicability of functionalization approaches for mesoporous hosts, the selected functional groups X (X = C_3H_6H, $C_3H_6NH_2$, $C_3H_6NHCONH_2$ and C_3H_6COOH) in this work are covalently attached to silica surface by postsynthesis grafting. The SBA-15 material was first synthesized[7] and activated using standard activation procedure for silica surface[39] to generate more active silanol groups. As can be seen from the SEM image (Figure 1), the SBA-OH material consists of rope-knots-like aggregates. The rope length ranges between 2 and 4 μm. The TEM image reveals that SBA-OH has well-ordered 1-D mesopores arraying along the long axis with the pore size of ~8 nm. In the XRD patterns (Figure 2), better-resolved XRD diffraction displaying (100), (110), and (200) reflections in *p6mm* symmetry is observed for SBA-OH (Figure 2b) than for calcined SBA-15 (Figure 2a), which is consistent with observed previously by Huo et al.[40] They found that the postsynthesis hydrothermal treatment improved the ordered structures of surfactant-containing MCM-41 and MCM-48. But the activation process gives rise to a decrease in both specific surface area and pore volume (as can be seen in Table 1), which is proposed to result from the partial elimination of micropores in the hydrothermal treatment. The XRD patterns characteristic of long-range ordered *p6mm* symmetry (Figure 2) and the nitrogen sorption isotherms typical of type IV (Figure 3A) are well retained in the functionalization, indicating that the grafting modification brings no damage to the ordered mesoporous structure of SBA-15. The surface area and pore volume are reduced in the functionalization by postsynthesis grafting (Table 1), which is more marked for SBA-$C_3H_6NH_2$ and SBA-$C_3H_6NHCONH_2$ than for SBA-C_3H_6H and SBA-C_3H_6COOH. This observed reduction is supposed to originate from the attachment of the desired organic group to the pore surface. The pore size distribution is almost as narrow as that before grafting, as shown in Figure 3B. But the pore size at maxi-

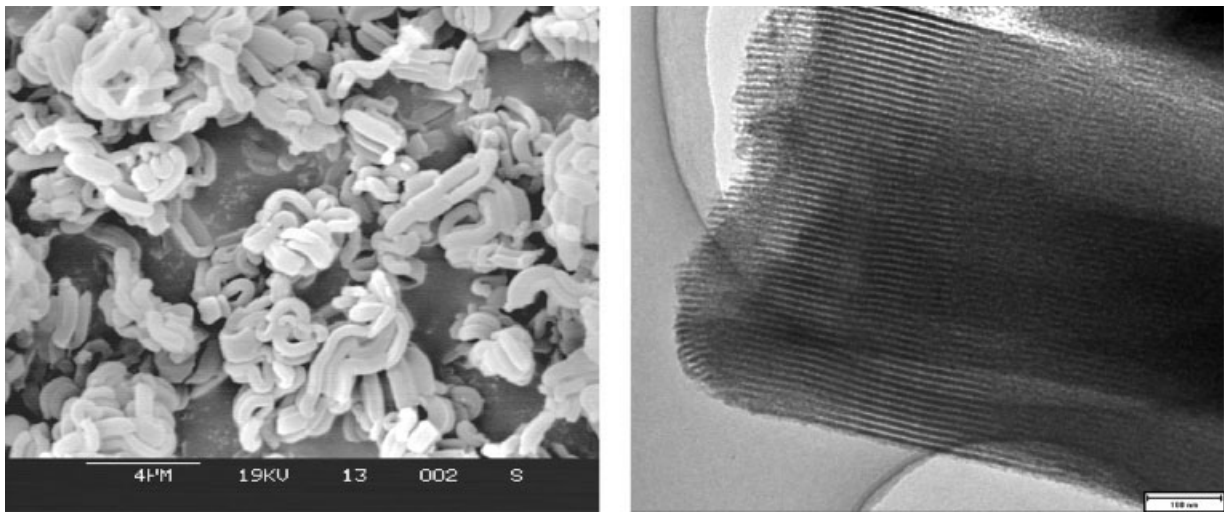

Figure 1. SEM (left) and TEM (right) images of SBA-OH.

mum distribution is reduced from 7.7 nm to around 6.6 nm for SBA-C_3H_6H, SBA-$C_3H_6NH_2$ and SBA-C_3H_6COOH, whilst to 5.5 nm for SBA-$C_3H_6NHCONH_2$ (see Table 1). The larger —$NHCONH_2$ moiety accounts for the more shrinkage of the pore size for SBA-$C_3H_6NHCONH_2$.

In the ^{29}Si MAS NMR spectrum of SBA-OH, three chemical shifts corresponding to Q^2 [$(SiO)_2Si(OH)_2$], Q^3[$(SiO)_3Si(OH)$], and Q^4 [$(SiO)_4Si$] are observed at −89, −99, and −109 ppm, respectively. According to the relative content of Q^2, Q^3 and Q^4 moieties, estimated from the integral areas of NMR peaks, the molecular formula of SBA-15-OH is written as $H_{0.3500}O_{2.175}Si$, giving a silanol group density of 5.7/nm^2. Based on the content of nitrogen or carbon (if no nitrogen atom in the grafted functional groups) element, the chain density of surface functional groups was estimated. The results are shown in Table 1. The coverage of —Si—$C_3H_6NH_2$ is estimated to be nearly complete from the chain density, while the coverage of —Si—C_3H_6H and —Si—C_3H_6COOH is most probably lower than 1, taking into consideration that not all silane moieties are grafted to the SBA-15 surface in T^3 linkage. The higher contents of grafted groups in SBA-$C_3H_6NH_2$ and SBA-$C_3H_6NHCONH_2$ are consistent with their more losses of surface areas and pore volumes caused by the functionalization. The dominating moieties on the surfaces of functionalized SBA-15 under various pH conditions are analyzed according to pK_a of the corresponding functional groups and shown in Table 2. The surface charge characters of different supports could be qualitatively determined consequently. The SBA-OH surface is negatively and SBA-$C_3H_6NHCONH_2$ surface is positively charged at all pH values investigated. SBA-$C_3H_6NH_2$ surface is positively charged at pH of 4.8 and 6.8 but approaches neutral at pH of 10.0 and 12.0. The SBA-C_3H_6COOH surface is approximately neutral at a pH of 4.8 but negatively charged at higher pH values. The —C_3H_6H group on SBA-C_3H_6H is not charged. But the SBA-C_3H_6H surface might be partially negatively charged because of the residual Si—OH.

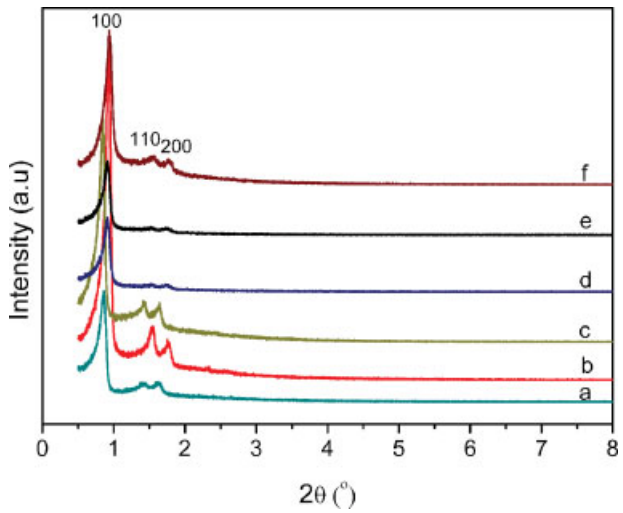

Figure 2. XRD patterns of (a) calcined SBA-15; (b) SBA-OH; (c) SBA-C_3H_6H; (d) SBA-$C_3H_6NH_2$; (e) SBA-$C_3H_6NHCONH_2$; (f) SBA-C_3H_6COOH.

[Color figure can be viewed in the online issue, which is available at www.interscience.wiley.com.]

Adsorption of Lz

Lz is a prolate spheroid protein with two characteristic cross sections of 3.0 × 4.5 and 3.0 × 3.0 nm^2, a molecular weight of 14.4 kDa, a stable structure between pH = 1.5 and

Table 1. Textural Properties of Pristine and Functionalized SBA-15 Materials

Sample	Specific Surface Area (m^2/g)	Pore Size (nm)	Pore Volume (cm^3/g)	The Density of Functional Groups (number/nm^2)
SBA-15, calcined	792	7.8	1.62	–
SBA-OH	588	7.7	0.90	5.7
SBA-C_3H_6H	511	6.6	0.79	1.9
SBA-$C_3H_6NH_2$	236	6.6	0.51	6.1
SBA-$C_3H_6NHCONH_2$	313	5.5	0.63	3.8
SBA-C_3H_6COOH	449	6.5	0.85	2.0

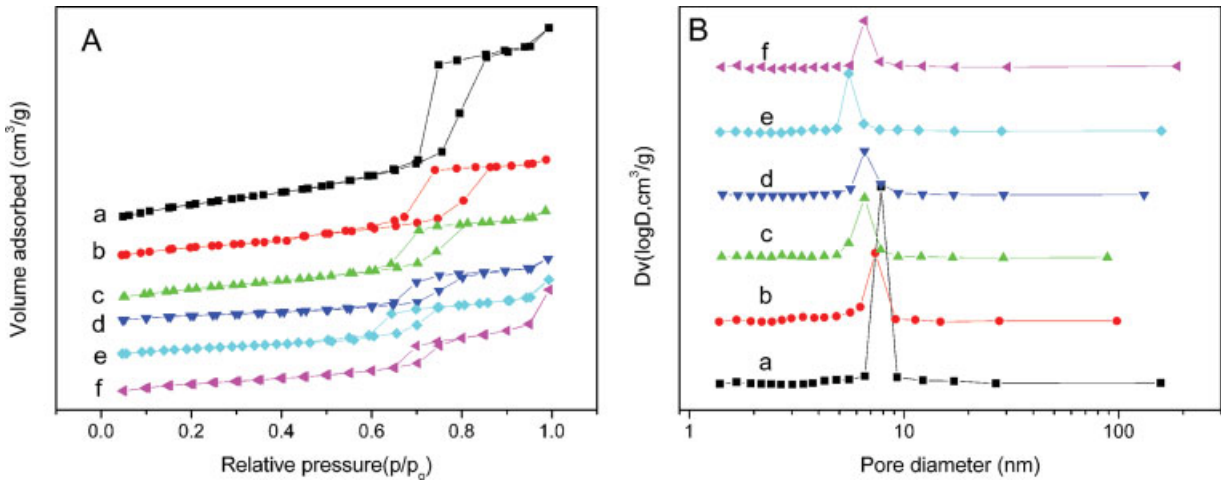

Figure 3. Nitrogen sorption isotherms (A) and pore size distribution (B) of (a) calcined SBA-15; (b) SBA-OH; (c) SBA-C_3H_6H; (d) SBA-$C_3H_6NH_2$; (e) SBA-$C_3H_6NHCONH_2$; (f) SBA-C_3H_6COOH.

[Color figure can be viewed in the online issue, which is available at www.interscience.wiley.com.]

12, and a pI of 11. The net charges of Lz molecules at pH = 4.8, 6.8, 10, and 12 have been reported to be +10, +8, +6, and −4,[41] respectively.

Adsorption Kinetics of Lz. The adsorption of proteins in nanoporous supports is a complex phenomenon involving multiple steps that occur simultaneously: (1) Transport to the surfaces by diffusion, which could be generally enhanced through mixing and shearing action. (2) Pore diffusion, the rate-limiting step when strong interfacial interactions occur (the protein adsorbed to the binding sites remains fixed), and hence mainly depending on the relative size of pores and protein molecules. (3) Adsorption/desorption at the surface, affected by the nature of surface–protein interactions, and described by an interfacial chemical reaction and its related kinetic adsorption and desorption mechanisms. (4) Surface diffusion, influenced mainly by the surface–protein interactions and negligible in the case of strong adsorption (no desorption occurs). (5) Conformational alteration of proteins in contact with the interface, and interactions with other adsorbed protein molecules. Supposing that no interaction is involved and the limited diffusion of Lz within the SBA-15 channels is controlled only by the spatial factor, the maximal average diffusion time for Lz (from the beginning to the end of channel opening) can be approximately calculated[42] by

$$t = \frac{L^2}{D_e} \tag{1}$$

wherein t is the diffusion time, L is the diffusion path with the maximum equal to the channel length, and D_e is the effective diffusion coefficient. D_e could be calculated by Eq. 2 in the case of $0 \le r/R = \lambda \le 0.95$.[43]

$$\frac{D_e}{D_0} = 1 + \frac{9}{8}\lambda \ln\lambda - 1.56034\lambda + 0.528155\lambda^2 + 1.91521\lambda^3 - 2.81903\lambda^4 + 0.270788\lambda^5 + 1.10115\lambda^6 - 0.435933\lambda^7 \tag{2}$$

wherein D_0 is the bulk solution diffusion coefficient; r is the Stokes–Einstein molecule radius of Lz, and R is the pore radius. In this system, L can be approximately regarded as the mean particle size (~4 μm). $D_0 = 1.2 \times 10^{-10}$ m^2/s and $r = 1.8$ nm.[44] R is taken as 2.75 nm, the smallest one among the pore radii for the supports investigated in this work. Taking these parameters to (1) and (2), the intraparticle diffusion time for Lz is estimated to be not longer than 1447 s. But actually the adsorption process is prolonged to more than 10 h (as indicated later in Figure 4) because of the occurrence of surface–protein and protein–protein interactions as well as conformation alterations of proteins in contact with interfaces. The interfacial interactions hinder the protein diffusion within the support pores. So the roles of interfacial interactions in the heterogeneity of adsorption kinetics are to be discussed principally.

Figure 4 shows the adsorption rate of Lz on SBA-15 as a function of time when the silica/Lz is 1.5 (w/w) under pHs of 4.8, 6.8, 10, and 12, respectively. The kinetic behaviors of Lz adsorption are basically similar under various pH on all the supports with different surface groups in that they all dis-

Table 2. Surface Moieties of Functionalized SBA-15 Materials Dominant at Different pH Conditions

Supports	Functional Groups	pH = 4.8	pH = 6.8	pH = 10.0	pH = 12.0
SBA-OH	$[-SiO^-]/[-SiOH]$	$10^{1.8}$	$10^{3.8}$	10^{7}	10^{9}
SBA-$C_3H_6NH_2$	$[-NH_3^+]/[-NH_2]$	$10^{5.6}$	$10^{3.6}$	$10^{0.37}$	$10^{-1.6}$
SBA-$C_3H_6NHCONH_2$	$[[-NHCONH_2]H^+]/[-NHCONH_2]$	$10^{9.4}$	$10^{7.4}$	$10^{4.2}$	$10^{2.2}$
SBA-C_3H_6COOH	$[-COO^-]/[-COOH]$	$10^{0.03}$	10^{2}	$10^{3.2}$	$10^{5.2}$

pK_a (Si−OH) = 3.6, pK_a (−C_3H_6−COOH) = 4.8, pK_a (−C_3H_6−NH_2) = 10.4, pK_a (−C_3H_6−$NHCONH_2$) = 14.2.

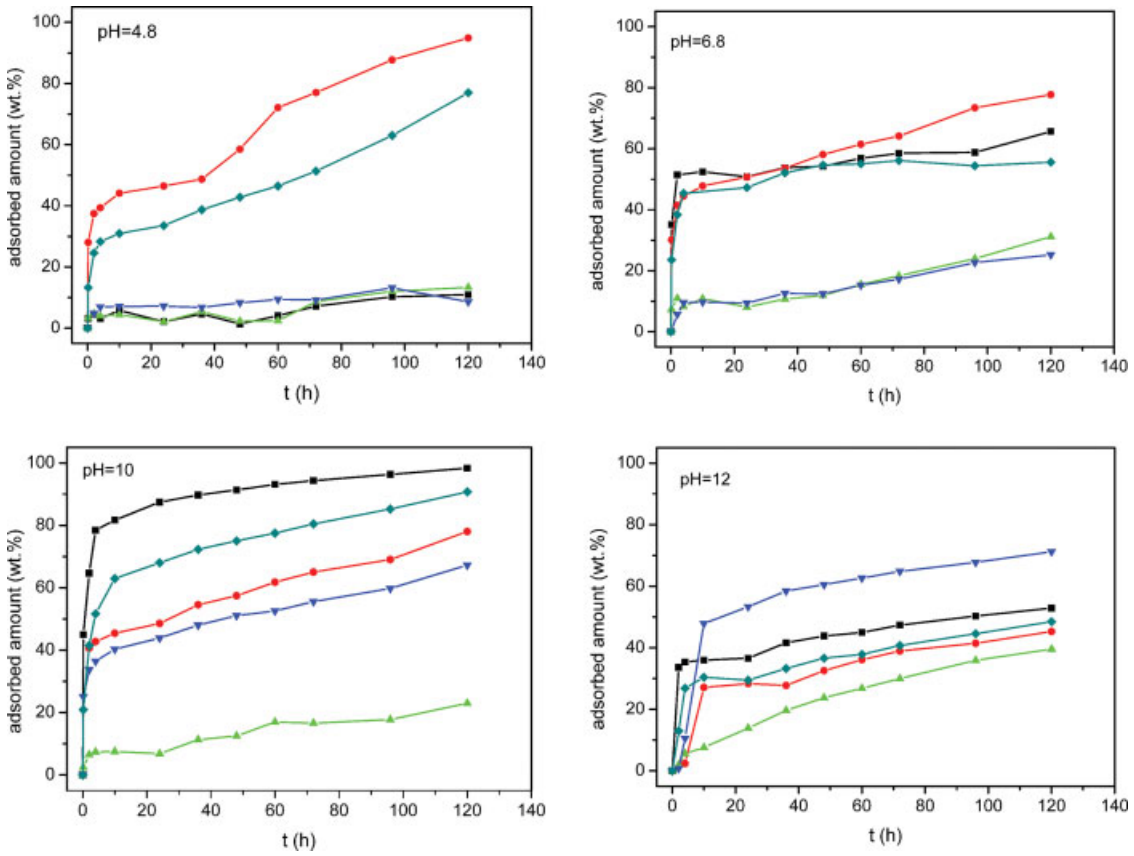

Figure 4. Adsorption rate of Lz on (■) SBA-OH; (●) SBA-C_3H_6H; (▲) SBA-$C_3H_6NH_2$; (▼) SBA-$C_3H_6NHCONH_2$; (◆) SBA-C_3H_6COOH at a pH of 4.8, 6.8, 10, and 12, respectively.

[Color figure can be viewed in the online issue, which is available at www.interscience.wiley.com.]

play distinct stages. In the first stage, the adsorption amount reaches a plateau rapidly generally within 10 h. But the adsorption amount at the plateau (maximal amount achieved in the first stage) exhibits great diversity depending on the surface group of the support and pH of the adsorption solution. So is the change trend of adsorption course in the second stage (after the plateau). At pH = 4.8, the Lz adsorption on either SBA-C_3H_6H or SBA-C_3H_6COOH shows a rapid initial rate indicating high affinity of Lz to the support surface, and then increases slowly with time. But the adsorption amounts on other three supports are quite low, and show almost no further changes with time. At pH = 6.8, a rapid initial Lz adsorption is observed on SBA-OH in addition to on SBA-C_3H_6H or SBA-C_3H_6COOH. Elevating pH to 10, the rapid adsorption is observed on all supports, except for on SBA-$C_3H_6NH_2$. Increasing pH further to 12, the Lz adsorption on SBA-$C_3H_6NHCONH_2$ becomes the fastest one, different from observed under other pH. Although the Lz adsorption amounts under the same pH are diverse on different supports, no close relationship could be found between the initial adsorption rate or adsorption amount and the support textural structures such as pore size, pore volume, and surface area. The observed difference in the initial adsorption rate should be well explained by the nature of the interfacial surface–protein interactions shown in Table 3. The charge repulsion results in slower adsorption rates, while either charge attraction, hydrophobic interaction, or certain hydrogen bonding serves as a driving force for Lz adsorption, as

Table 3. Surface–Protein Interactions Dominant at Various pH Conditions on Different Supports*

pH	SBA-OH	SBA-C_3H_6H	SBA-$C_3H_6NH_2$	SBA-$C_3H_6NHCONH_2$	SBA-C_3H_6COOH
4.8	Charge attraction	Hydrophobic	Charge repulsion	Charge repulsion	Hydrogen bonding + charge attraction
6.8	Charge attraction	Hydrophobic	Charge repulsion	Charge repulsion + π-π overlap	Charge attraction
10.0	Charge attraction	Hydrophobic	Hydrogen bonding + charge repulsion	Charge repulsion + π-π overlap	Charge attraction
12.0	Charge repulsion	Hydrophobic	Hydrogen bonding	Charge attraction + π-π overlap	Charge repulsion

**Based on the charge characters of support surfaces and lysozyme.

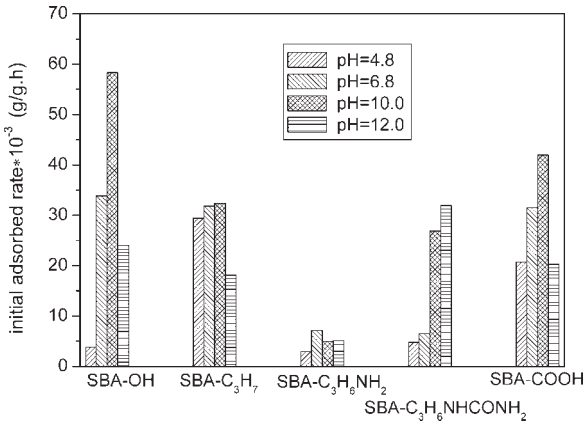

Figure 5. Dependence of initial adsorption rate on pH.

can be clearly observed in Figure 4. It is surprising that the hydrogen bonding between surface $-C_3H_6NH_2$ and Lz is not strong enough to drive Lz adsorption. At pH = 12, the adsorption rate on SBA-$C_3H_6NH_2$ is even slower than on SBA-OH and SBA-C_3H_6COOH where charge repulsion exists. The adsorption rate on SBA-C_3H_6H driven by hydrophobic interaction is also similar to that on SBA-OH and SBA-C_3H_6COOH. It has also to be noted that the adsorption rates on SBA-OH at pH = 4.8 and on SBA-$C_3H_6NHCONH_2$ at pH = 10 are the exceptions. The role of π-π overlapping of $-NHCONH_2$ and Lz surface has to be taken into consideration for SBA-$C_3H_6NHCONH_2$, and the occurrence of Lz adsorption on SBA-OH at pH = 4.8 is hindered by the lateral charge repulsion between proteins, which would be discussed respectively later.

The dependence of Lz adsorption rate on the nature of surface–protein interfacial interaction is observed more clearly in Figure 5, which illustrates the dependence of initial adsorption rate on pH for different supports. It can be seen from Figure 5 that the initial adsorption rate increases along with pH for SBA-$C_3H_6NHCONH_2$ and changes hardly for SBA-$C_3H_6NH_2$, while shows a maximum at pH = 10 for SBA-OH, SBA-C_3H_6H, and SBA-C_3H_6COOH. As shown in Table 3, the dominant interfacial interaction for SBA-OH and Lz is the electrostatic attraction between negatively charged surface and positively charged protein at a pH lower than 11 (pI of Lz), and then turns to electrostatic repulsion at pH = 12. As a result, the initial adsorption rate on SBA-OH displays a decrease when the adsorption pH increases from 10 to 12. Similar is the initial adsorption rate on SBA-C_3H_6COOH. In the SBA-C_3H_6COOH and Lz system, the dominant surface–protein interaction transforms from hydrogen bonding at pH = 4.8 to charge attraction at pH = 6.8 and 10, and finally to charge repulsion at pH = 12. For SBA-C_3H_6H, the hydrophobic affinity predominates over the surface–protein interactions. As a result, the initial adsorption rate changes hardly with pH when pH $\leq$ 10. The decrease at pH = 12 could be attributed to the repulsive force from residual $Si-O^-$ because of a less than 1 coverage of grafted $-C_3H_6H$. For SBA-$C_3H_6NHCONH_2$, the surface–protein electrostatic repulsion dominates at pH = 4.8 and 6.8, resulting in similarly slow adsorption rates. Although the surface–protein charge repulsion is still present at pH = 10, a distinct increase in the initial adsorption rate is observed, suggesting that some surface–protein affinity become dominant. The affinity is believed to arise from the π-π overlapping of $-NHCONH_2$ and Lz surface because of the similarity of —NHCO— moiety in $-C_3H_6NHCONH_2$ group to the peptide bonds in proteins. The surface charge of Lz decrease at a pH close to pI, which causes the weakening of the surface–protein charge repulsion. The affinity between the SBA-$C_3H_6NHCONH_2$ surface and Lz is, therefore, strong enough to counteract the charge repulsion at pH = 10. The charge attraction of surface–protein at a pH higher than pI contributes to the further increase in adsorption rate. For SBA-$C_3H_6NH_2$, an increase in initial adsorption rate should be observed at a pH higher than 10 because the surface–protein interaction transforms from charge repulsion to hydrogen bonding. But what is observed deviates from this deduction, implying that the hydrogen bonding between Lz and SBA-$C_3H_6NH_2$ is not sufficient or strong enough to drive Lz adsorption.

It can also be observed from Figure 5 that the adsorption rate on SBA-OH is severely influenced by adsorption pH even though the nature of surface–protein interaction is the same when pH $\leq$ 10. An exceptionally low adsorption rate is observed at pH = 4.8 despite the presence of electrostatic driving force. But the adsorption rate shows a marked increase along with pH in the case of charge attraction. This kind of pH effects is consistent with the ones reported previously by Vinu et al.[17,24,27] They proposed that the lateral repulsion between Lz greatly reduced the adsorption amount. It has been reported that the area per molecule of Lz in solution having a pH near the isoelectric point is similar to the area per molecule of Lz in its crystallized state (13.5 nm^2), whereas it doubles to 26.6 nm^2 at a solution pH of 4.[45] The adsorption rate on SBA-OH decreases in more than double when pH changes from 10 to 4.8 as shown in Figure 5. However, this pH effect appears limited to the supports where the electrostatic driving forces are involved. The dependence of adsorption rate on pH lessens slightly on SBA-COOH support (pH = 6.8 and 10). In the case of SBA-C_3H_6H (pH $\leq$ 10) and SBA-$C_3H_6NH_2$ where van der Waals (hydrophobic affinity or hydrogen bonding) is dominant for driving forces, the initial adsorption rate changes hardly with pH. So it is more rational to deduce that the protein–protein lateral repulsion contributes dependently on the surface–protein interactions. That is, in another word, related to surface diffusion of proteins. When the surface–protein interaction is strong, electrostatic attraction for example, the surface diffusion of the protein already adsorbed is slowed down, or even no surface diffusion occurs. As a result, more is the protein–protein lateral repulsion, more is the successive protein adsorption hindered. When Lz is adsorbed on the surface by van der Waals, the surface diffusion is much easier. So the adsorption pH influences little on the initial adsorption rate. The observed slow adsorption following the initial rapid process on SBA-C_3H_6H or SBA-C_3H_6COOH at pH = 4.8, different from observed on other supports and under other pH, could also be rationally explained by the surface diffusion and protein–protein repulsion mentioned earlier.

Adsorption Equilibrium of Lz. The Lz adsorption isotherms determined at pH = 6.8 and 10 are illustrated in Figures 6 and 7, respectively. As shown in Figure 6, the adsorp-

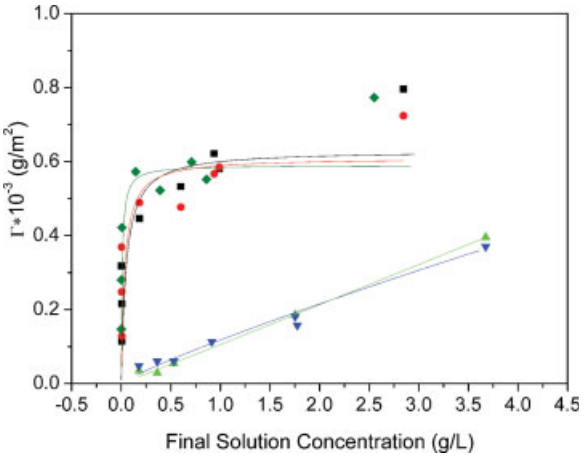

Figure 6. Sorption isotherms of Lz at pH = 6.8 and *T* = 298 K on (■) SBA-OH; (●) SBA-C_3H_6H; (▲) SBA-$C_3H_6NH_2$; (▼) SBA-$C_3H_6NHCONH_2$; (◆) SBA-C_3H_6COOH.

The data points are experimentally determined, and the curves are simulated. [Color figure can be viewed in the online issue, which is available at www.interscience.wiley.com.]

tion isotherms of Lz at pH = 6.8 on SBA-OH, SBA-C_3H_6H, and SBA-C_3H_6COOH display L-type, characteristic of a high affinity between Lz and the adsorbent surface. The high surface–protein affinity causes a sharp initial rise in adsorption amount. The isotherms on SBA-$C_3H_6NH_2$ and SBA-$C_3H_6NHCONH_2$ show S-type characteristic of weak surface–protein affinity because the charge repulsion predominates over the surface–protein interactions. The rise of adsorption amount at higher Lz concentration is driven by protein–protein aggregation. Increasing the adsorption pH from 6.8 to 10 changes the adsorption isotherm on SBA-$C_3H_6NHCONH_2$ to L-type displaying a sharp initial rise, as can be seen in Figure 7, because of the transformation of surface–protein repulsion to high affinity by π-π overlapping. Although the surface–protein interaction turns to hydrogen bonding from charge repulsion for SBA-$C_3H_6NH_2$, the adsorption isotherm still shows S-type representing a weak surface–protein affinity. The steady-state is more difficult to reach for the adsorption at pH = 6.8 than at pH = 10 as can be seen from the comparison of Figures 6 and 7, in accordance with the stronger protein repulsion at lower pH. The lateral repulsion between proteins is supposed to work more at high coverage. The observations by the adsorption isotherms are well con-

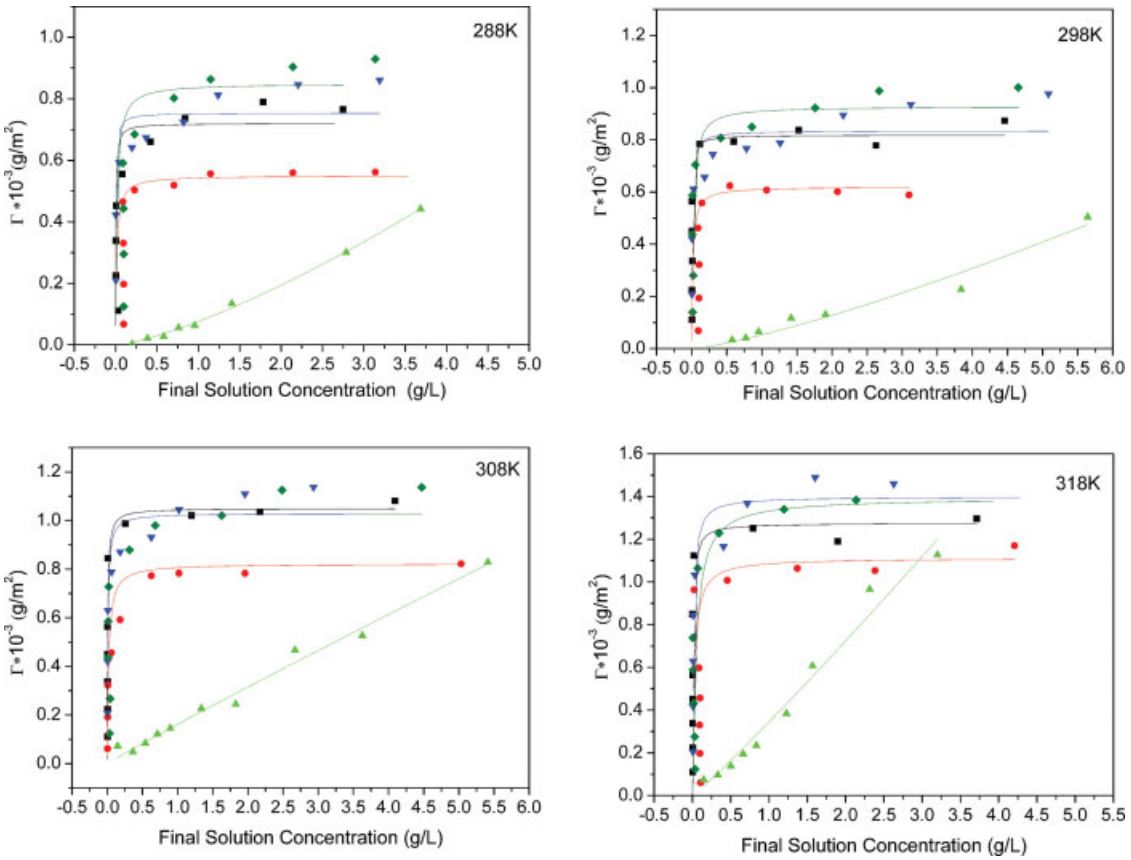

Figure 7. Sorption isotherms of Lz at pH = 10 on (■) SBA-OH; (●) SBA-C_3H_6H; (▲) SBA-$C_3H_6NH_2$; (▼) SBA-$C_3H_6NHCONH_2$; (◆) SBA-C_3H_6COOH at 288, 298, 308, 318 K, respectively. The data points are experimentally determined, and the curves are simulated.

[Color figure can be viewed in the online issue, which is available at www.interscience.wiley.com.]

sistent with that in the study of adsorption kinetics mentioned earlier.

As can be distinguished from Figure 7, the electrostatic adsorption of Lz on SBA-OH and hydrophobic adsorption on SBA-C_3H_6H are more readily to achieve equilibrium than on SBA-C_3H_6COOH and SBA-$C_3H_6NHCONH_2$. This is probably due to the roles of dependent conformational alterations of proteins. It is well known that the electrostatic force is long-distance while van der Waals forces are short-range interactions. Among the van der Waals forces, the hydrophobic affinity between alkyl chains is less orientational and direction-selective than π-π overlapping and hydrogen bonding. The occurrence of π-π overlapping or hydrogen bonding requires the directed close-up or contact of proteins to support surfaces. To be adsorbed by π-π overlapping, the proteins have to experience conformational change on the surfaces, accounting for the prolongation of adsorption equilibrium on SBA-$C_3H_6NHCONH_2$. The equilibrium detention on SBA-C_3H_6COOH indicates that there exist van der Waals interactions between surface terminal $-COO^-$ and Lz in addition to the electrostatic attraction.

The L-type isotherms are described by pseudo-Langmuir sorption Eq. 3, and S-type isotherm by Freundlich model (4).

$$\frac{\Gamma}{\Gamma_m} = \frac{K_L C}{1 + K_L C} \tag{3}$$

$$\Gamma = K_F C^{1/n} \tag{4}$$

wherein K_L and K_F are Langmuir and Freundlich parameters, respectively, C is the Lz concentration remaining in solution, Γ_m is the monolayer adsorption capacity, Γ is the adsorbed amount determined experimentally, and n is the nonlinear coefficient. The simulation plots are shown in Figures 6 and 7 together with experimental data points. The Langmuir model fits the L-type isotherms at pH = 10 better than at pH = 6.8. The experimental points at pH = 10 for SBA-OH and SBA-C_3H_6H are described by Langmuir equation better than for SBA-C_3H_6COOH and SBA-$C_3H_6NHCONH_2$. The deviation of simulated Langmuir plots from experimental data at high coverage is attributed to the adsorption retardation by protein–protein repulsion or Lz conformational alterations. From the simulated plots, the corresponding parameters are estimated and given in Table 4. Because the adsorbed amount continuously changes with time without exhibiting a clear plateau in some cases (as can be seen in Figure 4), a genuine steady-state is hard to reach. So the Γ_m is actually an adsorbed amount in quasi-steady state where the change of adsorbed amount with time or Lz concentration turns into gentle. As shown in Table 4, the calculated Γ_m fits well with the initial adsorption amount determined from $\Gamma \sim t$ curve. Elevating the adsorption pH from 6.8 to 10, the quasi-steady adsorption amounts on SBA-OH and SBA-C_3H_6COOH increase, while that on SBA-C_3H_6H hardly changes. This further confirms the conclusion in the discussion of kinetics that the protein–protein repulsions play a role not independently of the nature of surface–protein interactions.

The parameter K_L or K_F at 288, 298, 308, and 318 K is also estimated, respectively, from the sorption isotherms at pH = 10 (Figure 7) and given in Table 4. According to

Table 4. Γ_m and K_L in Langmuir Model, K_F and n in Freundlich Equation, ΔH in the Sorption, Quasi-Steady Distribution of Lz, and $\Gamma_{initial}$ from $\Gamma \sim t$ Curves for Comparison

	pH = 6.8				pH = 10.0										
	298 K			288 K			298 K			308 K			318 K				
	$\Gamma_{initial}$ (10^{-3} g/m^2)	Γ_m* (10^{-3} g/m^2)	K_L† (L/g)	Γ_m‡ (10^{-3} g/m^2)	K_L§ (L/g)	$\Gamma_{initial}$ (10^{-3} g/m^2)	Γ_m‡ (10^{-3} g/m^2)	K_L§ (L/g)	Γ_m‡ (10^{-3} g/m^2)	K_L§ (L/g)	Γ_m‡ (10^{-3} g/m^2)	K_L§ (L/g)	ΔH (kJ/mol)	Lz Number Adsorbed on per 100 nm^2 Solid Surface at 318 K
SBA-OH	0.58	0.63	40	0.72	231	0.99	0.82	173	1.05	140	1.28	116	−16	5.18
SBA-C_3H_6H	0.62	0.61	28	0.55	70	0.63	0.62	60	0.82	40	1.11	25	−15	4.43
SBA-$C_3H_6NH_2$	0.30	0.10	0.99	0.07	0.75	0.21	0.05	0.79	0.16	0.96	0.34	0.93	+77	0.88¶
SBA-$C_3H_6NHCONH_2$	0.21	0.12	1.15	0.75	244	0.86	0.83	125	1.03	113	1.40	77	−27	6.02
SBA-C_3H_6COOH	0.70	0.59	100	0.85	60	0.93	0.93	50	1.05	28	1.39	22	−33	5.68

*K_F in Freundlich equation for SBA-$C_3H_6NH_2$ and SBA-$C_3H_6NHCONH_2$.
†n in Freundlich equation for SBA-$C_3H_6NH_2$ and SBA-$C_3H_6NHCONH_2$.
‡K_F in Freundlich equation for SBA-$C_3H_6NH_2$.
§n in Freundlich equation for SBA-$C_3H_6NH_2$.
¶Based on initial adsorption amount.

Eq. 5, the parameter K could be correlated with the sorption enthalpy. The ΔH in the Lz sorption on various supports, obtained from the plots of ln K vs. $1/T$, accords well with the surface–protein interactions (pH = 10). The high affinity of SBA-OH, SBA-C_3H_6H, SBA-$C_3H_6NHCONH_2$, and SBA-C_3H_6COOH to Lz results in an exothermic sorption, while the sorption of Lz on SBA-$C_3H_6NH_2$ appears endothermic. But all the thermal effects are not strong as a result of noncovalent surface–protein interactions.

$$\ln K = \frac{\Delta S}{R} - \frac{\Delta H}{RT} \tag{5}$$

It is interesting to note that the hydrophobic affinity, π-π overlapping, and hydrogen bonding exhibit great difference in driving Lz adsorption, although they are all van der Waals. The hydrogen bonding between —C_3H_6COOH and Lz, hydrophobic affinity, and π-π overlapping favor the Lz adsorption concerning both the adsorption kinetics and adsorption isotherms. But the hydrogen-bonding force between SBA-$C_3H_6NH_2$ surface and Lz surface works less on the Lz adsorption, though it is a relatively strong van der Waals interaction. The significant role of π-π overlapping could rationally be associated with the extensive presence of peptide linkage on Lz surface. The significant role of hydrophobic affinity could be related to the appropriately hydrophobic Lz surface. The general distribution of side chains in proteins usually conforms closely to the pattern observed in myoglobin in that all of the ionizable groups and most of the polar side chains are distributed over the molecule surface, while the majority of the apolar side chains lie within its interior.[46] But for most small globular proteins, the apolar atoms occupy between 40% and 60% of the water-accessible surface area, which gives the proteins relatively high surface hydrophobicity.[46] For Lz, the apolar residues cover 59%[47] of the protein surface, which consists of hydrophobic tryptophan, isolcuci, and valine residues.[48] The hydrogen-bonding interaction between the terminal —NH_2 on support surface and polar arginine and lysine residues[48] on the exterior surface of protein seems relatively difficult, resulting in a less affinity and a slower initial adsorption rate.

Distribution and Adsorption Reversibility of Lz on the Support Surfaces. According to the sorption isotherms discussed earlier, the distribution states of Lz on the supports with different surface groups are depicted as follows. Lz is distributed on SBA-$C_3H_6NH_2$ in protein aggregates at both pH = 6.8 and 10. The distribution of Lz on SBA-OH, SBA-C_3H_6H, and SBA-C_3H_6COOH at both pH is all in monolayer. But the Lz density on SBA-OH and SBA-C_3H_6COOH increases when pH increases from 6.8 to 10. The Lz molecules on SBA-$C_3H_6NHCONH_2$ transform from multilayer aggregate to monolayer distribution as pH increases. The number of Lz adsorbed on per 100 nm^2 support surface at 318 K is estimated from the quasi-steady adsorption amount and shown in Table 4. 318 K is selected because at this temperature the L-type adsorption amount of Lz approaches fixed at high coverage.

The Lz adsorbed at pH = 6.8 and 10 on the SBA-15 supports with different surface modifications were leached in buffers to investigate the adsorption reversibility. The observed percentage desorption in each case indicates the adsorption of Lz is only partially reversible. The adsorbed Lz is leached in a ratio of less than 5%, as shown in Figure 8. Under the same adsorption and desorption conditions, the percentage desorption ratios of Lz in the tested candidates show a little diversity depending on the distribution states as well as the surface–protein interactions. Generally, the Lz adsorbed in multilayer aggregate is more readily to be leached. For example, the adsorption of Lz on SBA-$C_3H_6NHCONH_2$ at pH = 6.8 and on SBA-$C_3H_6NH_2$ at pH = 10 shows higher percentage desorption. Although Lz is all distributed in monolayer on SBA-OH, SBA-C_3H_6H, and SBA-C_3H_6COOH at pH = 6.8 and on SBA-OH, SBA-C_3H_6H, SBA-$C_3H_6NHCONH_2$, and SBA-C_3H_6COOH at pH = 10, the percentage desorption is higher for the adsorption by hydrophobic interaction or π-π overlapping than by charge attraction. The adsorption at pH = 6.8 is more reversible than at pH = 10 on all supports investigated here except for on SBA-$C_3H_6NH_2$, resulting from the larger contribution of protein–protein repulsion at a pH deviating more from pI.

FTIR Investigation of Lz Secondary Structure. Infrared spectroscopy is a useful technique to monitor the structural changes when the proteins were immobilized on the supports.[49] Figure 9 shows the FTIR spectra of Lz adsorbed on the modified SBA-15 supports. For comparison, the spectra for pristine support and Lz are also illustrated. The bands of Lz centered at 1655 cm^{-1} characteristic of amide I and around 1535 cm^{-1} of amide II are clearly observed after adsorption on different supports. For the adsorption on SBA-OH, SBA-C_3H_6H, and SBA-$C_3H_6NH_2$, the amide I and II bands show no changes in the absorption position. The band is observed at 1642 cm^{-1} and 1541 cm^{-1}, respectively, for SBA-$C_3H_6NHCONH_2$. The shift is supposed to result from the enveloped absorption of surface —$NHCONH_2$ groups. The —$NHCONH_2$ also has IR absorption at 1640–1650 cm^{-1} and 1510–1570 cm^{-1}, quite similar to that of proteins. The shift of the band at 1535–1555 cm^{-1} observed for SBA-C_3H_6COOH originates from the interfering of surface —COOH groups. The deprotonization of —COOH in the Lz adsorption (pH = 10) shifts its absorption from 1721 cm^{-1} to 1550–1610 cm^{-1}. The amide I band (1600–1700 cm^{-1}) arises from the α-helix, β-sheet, β-turn, and ran-

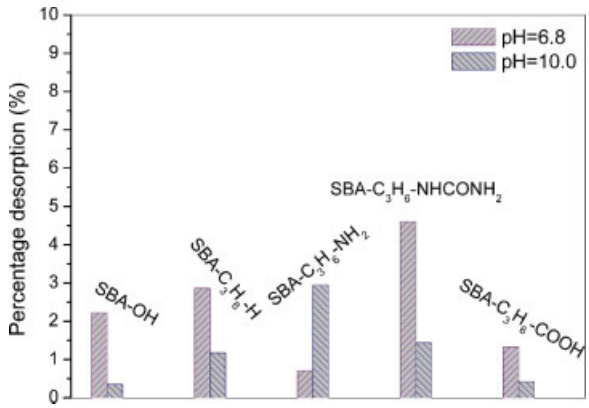

Figure 8. Partial reversibility of Lz adsorption.

[Color figure can be viewed in the online issue, which is available at www.interscience.wiley.com.]

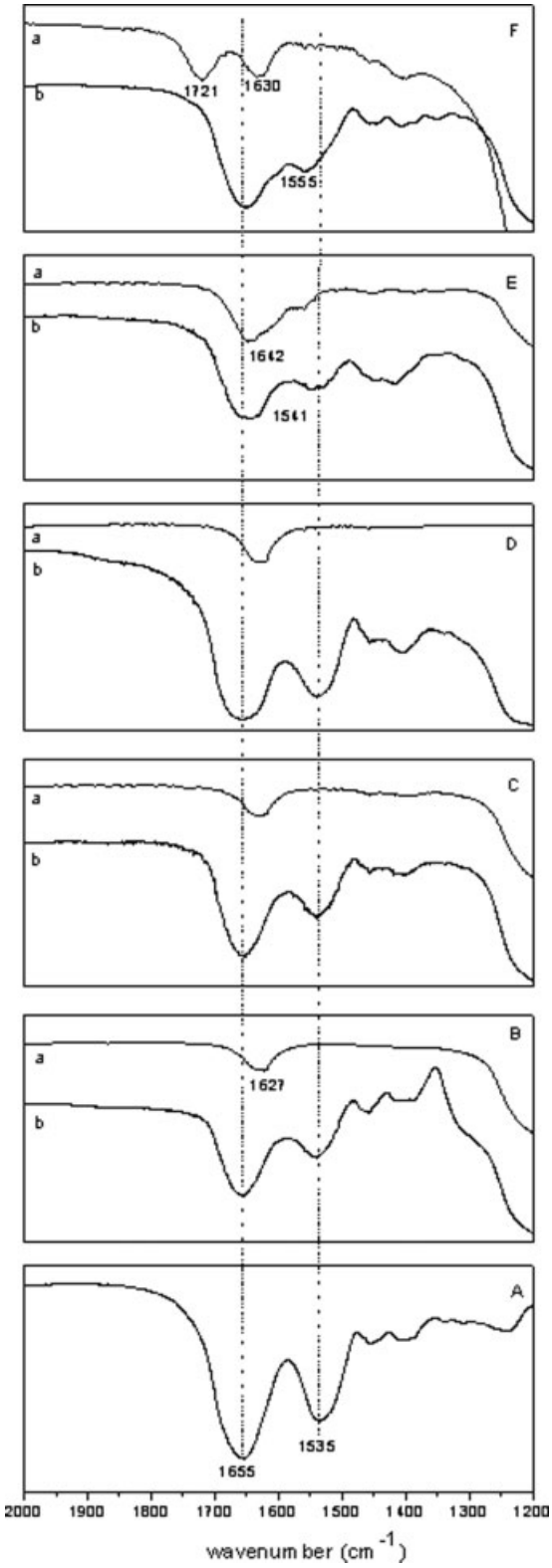

Figure 9. FTIR spectra of (A) Lz powder and (B) SBA-OH; (C) SBA-C_3H_7; (D) SBA-$C_3H_6NH_2$; (E) SBA-$C_3H_6NHCONH_2$; (F) SBA-C_3H_6COOH. (a) Without and (b) with Lz adsorbed.

dom coil in protein conformation, while the amide II band (1500–1600 cm^{-1}) is related to a combination of C—N stretching and N—H bending vibrations of the protein backbone, both of which image the protein secondary structure. The reserved and unvaried FTIR bands indicate that the adsorption of Lz on modified SBA-15 supports scarcely damages the secondary structure of Lz, which is significantly important for the protein storage, separation, and application as a biocatalyst.

Conclusions

In summary, the interfacial interactions play a significantly key role in the adsorption kinetics, adsorption capacity, distribution states and adsorption reversibility. In addition to the electrostatic force, hydrophobic interaction, and hydrogen bonding, the π-π overlapping is also a significantly crucial driving force for protein adsorption. But the hydrogen bonding between the surface NH_2 and Lz is exceptionally not sufficient to drive Lz adsorption. Different from the previous observations, our study demonstrates that the protein–protein repulsion makes impact dependently on the nature of surface–protein interactions. The protein–protein repulsion hinders the Lz diffusion more severely when strong surface–protein interactions occur. The organic modification of inorganic support surface reduces the dependence of protein adsorption on the protein–protein repulsion. The Lz distribution on the supports has also been found to be readily changed by tailoring the surface–protein interfacial interactions. Our findings in this work are believed to provide new information and great insights to the tuning of protein adsorption heterogeneities by tailoring the surface properties of solid supports, which is significantly crucial to generate the desired adsorption for protein immobilization, bioreactors, or bioseparation.

Acknowledgments

The authors are grateful to the financial support from NSFC, Program for Changjiang Scholars and Innovative Research Team in University (IRT0406), Program for New Century Excellent Talents in University (NCET-04-0119), and "111" Project (B07004).

Literature Cited

1. Kresge CT, Leonowicz ME, Roth WJ, Vartuli JC, Beck JS. Ordered mesoporous molecular sieves synthesized by a liquidcrystal template mechanism. *Nature*. 1992;359:710–712.
2. Beck JS, Vartuli JC, Roth WJ, Leonowicz ME, Kresge CT, Schmitt KD, Chu CTW, Olson DH, Sheppard EW, McCullen SB, Higgins JB, Schlenker JL. A new family of mesoporous molecular sieves prepared with liquid crystal templates. *J Am Chem Soc*. 1992;114:10834–10843.
3. Bagshaw SA, Prouzet E, Pinnavaia TJ. Templating of mesoporous molecular sieves by nonionic polyethylene oxide surfactants. *Science*. 1995;269:1242–1244.
4. Huo Q, Leon R, Petroff PM, Stucky GD. Mesostructure design with gemini surfactants: supercage formation in a three-dimensional hexagonal array. *Science*. 1995;268:1324–1327.
5. Tanev PT, Pinnavaia TJ. A neutral templating route to mesoporous molecular sieves. *Science*. 1995;267:865–867.
6. Zhao D, Feng J, Huo Q, Melosh N, Fredrickson GH, Chmelka BF, Stucky GD. Triblock copolymer syntheses of mesoporous silica with periodic 50 to 300 angstrom pores. *Science*. 1998;279:548–552.
7. Zhao D, Huo Q, Feng J, Chmelka BF, Stucky GD. Nonionic triblock and star diblock copolymer and oligomeric surfactant syntheses of highly ordered, hydrothermally stable, mesoporous silica structures. *J Am Chem Soc*. 1998;120:6024–6036.

8. Schmidt-Winkel P, Lukens WW, Zhao D, Yang P, Chmelka BF, Stucky GD. Mesocellular siliceous foams with uniformly sized cells and windows. *J Am Chem Soc*. 1999;121:254–255.
9. Diaz JF, Balkus KJ. Enzyme immobilization in MCM-41 molecular sieve. *J Mol Catal B: Enzymatic*. 1996;2:115–126.
10. Hartmann M. Ordered mesoporous materials for bioadsorption and biocatalysis. *Chem Mater*. 2005;17:4577–4593.
11. Katiyar A, Pinto NG. Visualization of size-selective protein separations on spherical mesoporous silicates. *Small*. 2006;2:644–648.
12. Han YJ, Stucky GD, Butler A. Mesoporous silicate sequestration and release of proteins. *J Am Chem Soc*. 1999;121:9897–9898.
13. M Kisler J, Dahler A, W Stevens G, J O'Connor A. *Microporous. Mesoporous. Mater*. 2001;44–45:769–774.
14. Yiu HHP, Botting CH, Botting NP, Wright PA. Size selective protein adsorption on thiol-functionalised SBA-15 mesoporous molecular sieve. *Phys Chem Chem Phys*. 2001;3:2983–2985.
15. Itoh T, Yano K, Inada Y, Fukushima Y. Stabilization of chlorophyll a in mesoporous silica and its pore size dependence basis of a presentation given at materials discussion No. 5, September 22–25, 2002, Madrid, Spain. *J Mater Chem*. 2002;12:3275–3277.
16. Deere J, Magner E, Wall JG, Hodnett BK. Mechanistic and structural features of protein adsorption onto mesoporous silicates. *J Phys Chem B*. 2002;106:7340–7347.
17. Vinu A, Murugesan V, Tangermann O, Hartmann M. Adsorption of cytochrome c on mesoporous molecular sieves: influence of pH, pore diameter, and aluminum incorporation. *Chem Mater*. 2004;16:3056–3065.
18. Fan J, Lei J, Wang LM, Yu CZ, Tu B, Zhao DY. Rapid and high-capacity immobilization of enzymes based on mesoporous silicas with controlled morphologies. *Chem Commun*. 2003;3:2140–2141.
19. Liu J, Li C, Yang Q, Yang J, Li C. Morphological and structural evolution of mesoporous silicas in a mild buffer solution and Lysozyme adsorption. *Langmuir*. 2007;23:7255–7262.
20. Lee J, Kim J, Kim J, Jia H, Kim M, Kwak JH, Jin S, Dohnalkova A, Park HG, Chang HN, Wang P, Grate JW, Hyeon T. Simple synthesis of hierarchically ordered mesocellular mesoporous silica materials hosting crosslinked enzyme aggregates. *Small*. 2005;1:744–753.
21. Muller-Dethlefs K, Hobza P. Noncovalent interactions: a challenge for experiment and theory. *Chem Rev*. 2000;100:143–168.
22. Sadana A. Protein adsorption and inactivation on surfaces. Influence of heterogeneities. *Chem Rev*. 1992;92:1799–1818.
23. Wang YJ, Caruso F. Mesoporous silica spheres as supports for enzyme immobilization and encapsulation. *Chem Mater*. 2005;17:953–961.
24. Vinu A, Miyahara M, Ariga K. Biomaterial immobilization in nanoporous carbon molecular sieves: influence of solution pH, pore volume, and pore diameter. *J Phys Chem B*. 2005;109:6436–6441.
25. Katiyar A, Ji L, Smirniotis P, Pinto NG. Protein adsorption on the mesoporous molecular sieve silicate SBA-15: effects of pH and pore size. *J Chromatogr A*. 2005;1069:119–126.
26. Hudson S, Magner E, Cooney J, Hodnett BK. Methodology for the immobilization of enzymes onto mesoporous materials. *J Phys Chem B*. 2005;109:19496–19506.
27. Vinu A, Murugesan V, Hartmann M. Adsorption of Lysozyme over mesoporous molecular sieves MCM-41 and SBA-15: influence of pH and aluminum incorporation. *J Phys Chem B*. 2004;108:7323–7330.
28. Yiu HHP, Wright PA. Enzymes supported on ordered mesoporous solids: a special case of an inorganic–organic hybrid. *J Mater Chem*. 2005;15:3690–3700.
29. Chong ASM, Zhao XS. Functionalized nanoporous silicas for the immobilization of penicillin acylase. *Appl Surf Sci*. 2004;237:398–404.
30. Yiu HHP, Wright PA, Botting NP. Enzyme immobilisation using siliceous mesoporous molecular sieves. *Micropor Mesopor Mater*. 2001;44–45:763–768.
31. Feng X, Fryxell GE, Wang LQ, Kim AY, Liu J, Kemner KM. Functionalized monolayers on ordered mesoporous supports. *Science*. 1997;276:923–926.
32. Stein A, Melde BJ, Schroden RC. Hybrid inorganic–organic mesoporous silicates-nanoscopic reactors coming of age. *Adv Mater*. 2000;12:1403–1419.
33. Hoffmann F, Cornelius M, Morell J, Froba M. Silica-based mesoporous organic–inorganic hybrid materials. *Angew Chem Int Ed*. 2006;45:3216–3251.
34. Sayari A, Hamoudi S. Periodic mesoporous silica-based organic-inorganic nanocomposite materials. *Chem Mater*. 2001;13:3151–3168.
35. Maria Chong AS, Zhao XS. Functionalization of SBA-15 with APTES and characterization of functionalized materials. *J Phys Chem B*. 2003;107:12650–12657.
36. Lei C, Shin Y, Liu J, Ackerman EJ. Entrapping enzyme in a functionalized nanoporous support. *J Am Chem Soc*. 2002;124:11242–11243.
37. Yiu HHP, Wright PA, Botting NP. Enzyme immobilisation using SBA-15 mesoporous molecular sieves with functionalised surfaces. *J Mol Catal B: Enzymatic*. 2001;15:81–92.
38. Balamurugan S, Ista LK, Yan J, Lopez GP, Fick J, Himmelhaus M, Grunze M. Reversible protein adsorption and bioadhesion on monolayers terminated with mixtures of oligo(ethylene glycol) and methyl groups. *J Am Chem Soc*. 2005;127:14548–14549.
39. Cass T, Ligler FS. *Immobilized Biomolecules in Analysis: A Practical Approach*. Oxford: Oxford University Press, 1998.
40. Huo QS, Margolese DI, Stucky GD. Surfactant control of phases in the synthesis of mesoporous silica-based materials. *Chem Mater*. 1996;8:1147–1160.
41. States DJ, Karplus M. A model for electrostatic effects in proteins. *J Mol Biol*. 1987;197:111–130.
42. Zhang S, Sun Y. Study on protein adsorption kinetics to a dye–ligand adsorbent by the pore diffusion model. *J Chromatogr A*. 2002;964:35–46.
43. Dechadilok P, Deen WM. Hindrance factors for diffusion and convection in pores. *Ind Eng Chem Res*. 2006;45:6953–6959.
44. Gutenwik J, Nilsson B, Axelsson A. Effect of hindered diffusion on the adsorption of proteins in agarose gel using a pore model. *J Chromatogr A*. 2004;1048:161–172.
45. Su TJ, Lu JR, Thomas RK, Cui ZF, Penfold J. The effect of solution pH on the structure of lysozyme layers adsorbed at the silica–water interface studied by neutron reflection. *Langmuir*. 1998;14:438–445.
46. Haynes CA, Norde W. Structures and stabilities of adsorbed proteins. *J Colloid Interface Sci*. 1995;169:313–328.
47. Lee B, Richards FM. The interpretation of protein structure: estimation of static accessibility. *J Mol Biol*. 1971;55:379–380.
48. Phillips DC. The hen egg-white lysozyme molecule. *Proc Natl Acad Sci USA*. 1967;57:484–495.
49. Gao L, Gao Q, Wang Q, Peng S, Shi J. Immobilization of hemoglobin at the galleries of layered niobate $HCa_2Nb_3O_{10}$. *Biomaterials*. 2005;26:5267–5275.

Manuscript received Feb. 20, 2008, and revision received May 8, 2008.